PAPER

Check for updates

Study on the importance of uniformity and nanoparticle size in ZIF-8 carbon nanoarchitecture for enhancing electrochemical properties†

Donggyun Kim, [ID] [a] Jinhyeon Park, [ID] [a] Seonghyeon Jung,[a] Jieun Jang,[a] Minsu Han,[b,c] Minjun Kim,[b] Wenkai Zhu, [ID] [d] Woo-Jin Song,[e] Yusuke Yamauchi [ID] [a,b,c] and Jeonghun Kim [ID] *[a]

Metal–organic framework (MOF)-derived carbons, known for their highly tunable structures, have attracted considerable attention for electrochemical applications. Efficient ion and electron transport, along with low electrode resistance, is critical for enhancing performance in these areas. To optimize MOF-derived carbons, we synthesize Zn-based zeolitic imidazolate framework (ZIF-8) nanocrystals with controlled sizes and a narrow size distribution, resulting in nanoporous polyhedral carbon structures. The sample is then subjected to carbonization to yield ZIF-8-derived carbon (ZIF-8-C) doped with hetero-atoms, and subsequently, performance evaluations of supercapacitors are conducted to assess their ion and electron transport properties. Larger particles exhibit greater capacitance loss at high scan rates or current densities, likely due to underutilization of pores for ion diffusion. Uniform particle sizes facilitate ordered packing, improving electron pathways compared to electrodes with non-uniform particles and yielding higher electrochemical performance despite similar specific surface areas. Notably, the electrode prepared with the smallest and most uniformly sized ZIF-8-C-m1 exhibits a specific capacitance of 206.4 F g^{-1} at 1 A g^{-1}, along with excellent rate capability and stability, retaining 99.7% of its capacitance after 10 000 cycles at 10 A g^{-1}. In a two-electrode system, it achieves an energy density of up to 19.4 W h kg^{-1} at a specific power of 350 W kg^{-1}. The results present here offer valuable insights into the utilization of nanoporous carbons across diverse electrochemical applications.

1. Introduction

Over the last several decades, the demand for energy storage devices has significantly increased.[1] To meet this demand, electrochemical energy storage has emerged as a promising solution, offering extended lifespan and versatility with the utilization of various materials.[2–4] Supercapacitors, which function through ion movement at the electrode–electrolyte interface or surface chemical reactions during charging and discharging, offer distinct advantages over batteries, including high power density, extended cycle life, and rapid charging capabilities.[5] To enhance the power and energy density of supercapacitors, significant research efforts have been directed towards the development of nanostructured electrode materials. Nanostructured materials based on carbon have attracted significant attention and have been extensively investigated over the past decade.[6,7] They are valued for their large surface area, excellent electrical conductivity, chemical stability, long cycling stability, and ability to store electric charge in the form of electrical double-layer capacitors.[8,9] Most carbon-based materials used in electrode materials are synthesized *via* carbonization processes (*i.e.*, high-temperature pyrolysis) with precursors, such as biomass, polymers, and metal–organic frameworks (MOFs). Among the precursors used for synthesizing carbon-based electrode materials, MOF-based precursors are particularly promising owing to their customizable porous structures and configurations.[10–12] The Zn-based zeolitic imidazolate framework (ZIF-8), an MOF, possesses adjustable pore sizes, high specific surface area, high crystallinity, uniform pore structure, and exceptional chemical and thermal stability.[13–17] Upon carbonization, ZIF-8 derived carbon (ZIF-8-C) exhibits a significantly high specific surface area and high

[a]Department of Chemical and Biomolecular Engineering, Yonsei University, Seoul 03722, Republic of Korea. E-mail: jhkim03@yonsei.ac.kr
[b]Australian Institute for Bioengineering and Nanotechnology (AIBN), The University of Queensland, Brisbane, Queensland 4072, Australia
[c]Department of Materials Process Engineering, Graduate School of Engineering, Nagoya University, Furo-cho, Chikusa-ku, Nagoya, Aichi 464-8603, Japan
[d]College of Chemistry and Materials Engineering, Zhejiang A&F University, Hangzhou 311300, China
[e]Department of Organic Materials Engineering, Chungnam National University, 99 Daehak-ro, Yuseong-gu, Daejeon, 34134, Republic of Korea
†Electronic supplementary information (ESI) available. See DOI: https://doi.org/10.1039/d5nr00556f

nitrogen content, making it suitable for various applications beyond electrochemical uses, such as catalysis, adsorption, and advanced oxidation processes.[18–25]

Enhancing the electrochemical properties of nano-sized MOF-based carbon materials with complex nanoporous structures is crucial. A key strategy for achieving this involves improving the kinetics and mass transport of the electrode.[26] This requires the consideration of three critical aspects: reducing electron transport length, minimizing ion diffusion distance, and ensuring easy accessibility of electrolyte ions.[27] Achieving the uniform packing of monodisperse carbon particles is a highly effective approach for realizing these goals, as it can significantly enhance electrode kinetics and mass transport.[28–30] However, maintaining particle uniformity while simultaneously controlling their size is significantly challenging.

Monodisperse ZIF-8 nanocrystals play a crucial role in creating uniform carbon particles. Several studies have investigated methods to regulate the particle size of ZIF-8 through the use of organic solvents or surfactants.[31] However, there are challenges in not only removing these substances from the pores but also with their cost and environmental impact. To address these disadvantages and overcome the drawbacks associated with organic solvents and surfactants, researchers have explored the water-based synthesis of ZIF-8 at room temperature.[32,33] Despite these efforts, simultaneously achieving both a wide range of size control and a narrow size distribution continues to present a considerable challenge.

In this study, we synthesized both monodisperse and polydisperse ZIF-8 nanocrystals to assess the impact of particle uniformity on electrochemical performance. We adjusted various synthesis parameters to obtain monodisperse particles of different sizes. Thereafter, these particles were carbonized under a N_2 flow to obtain N-doped carbon. The results revealed that all the ZIF-8-C samples retained their original size distribution after carbonization and exhibited similar specific surface areas and nitrogen contents. The electrochemical performance of the samples was comprehensively evaluated, with a focus on the detailed ion diffusion and electron transport characteristics relative to the particle size and distribution. Our findings revealed that smaller particle sizes and higher particle uniformity contributed to increased charge storage capacity and reduced electrode resistance. Additionally, larger particles contributed more significantly to reductions in capacitance at high scan rates or current densities, which may be attributed to the insufficient utilization of pores for ion diffusion. This research provides valuable insights into the optimization of particle size and uniformity for designing various MOF-based carbon materials with enhanced electrochemical performance.

2. Experimental section

2.1 Materials

Zinc acetate dihydrate $(Zn(OAc)_2 \cdot 2H_2O$, 99%), 2-methylimidazole (2-mIm) $(C_4H_6N_2$, 99%), hydrogen chloride (HCl),

sulfuric acid (H_2SO_4), poly(vinylidene fluoride) (PVDF), and N-Methyl-2-pyrrolidone (NMP) were purchased from Sigma-Aldrich. Deionized water (DIW) was used as the solvent. All chemicals were used as received without further purification.

2.2 Synthesis of ZIF-8 with different particle sizes

$Zn(OAc)_2$ (1.5 g, 0.273 M) and 2-mIm (6.73 g, 3.279 M) were individually dissolved in 25 mL of DIW. Thereafter, Zn solution was added to the 2-mIm solution over several seconds, and the resulting mixture was stirred at room temperature (750 rpm) for 15 min. Subsequently, the solution was aged for 24 h to obtain a white precipitate, which was then subjected to centrifugation (9000 rpm, 10 min) and washed five times with water. Thereafter, the ZIF-8 particles were dried for 24 h at 60 °C in a vacuum oven. To synthesize ZIF-8 particles with controlled sizes, the same procedure was followed, but the molar ratio, temperature, pouring time, and amount of water were adjusted. The resulting ZIF-8 samples were labeled as ZIF-8-mx, where x ranges from 1 to 5. To synthesize non-uniform ZIF-8 particles (denoted as ZIF-8-n), similar procedures were used, but the pouring order was changed (2-mIm solution to Zn solution), and the mixture was not subjected to vigorous stirring. A summary of the conditions for each sample is provided in Table S1.†

2.3 Preparation of ZIF-8-derived carbon

The prepared ZIF-8 powder was placed into a quartz boat and subjected to heating under a N_2 gas flow. The temperature was gradually increased up to 900 °C at a heating rate of 5 °C min^{-1} and maintained at that temperature for 3 h to facilitate carbonization. Subsequently, the ZIF-8-derived carbon powder was washed with a 2 M HCl solution to remove any residual Zn remaining after carbonization. Following the HCl wash, the powder was further washed five times with DIW and then dried in a vacuum oven at 60 °C for 24 h. The resulting ZIF-8-derived carbons were designated as ZIF-8-C-mx or ZIF-8-C-n, depending on the precursor ZIF-8.

2.4 Characterization

The surface morphologies and structures of the samples were characterized using field emission scanning electron microscopy (FE-SEM; JSM-7001F, JEOL Ltd, Japan) performed at 10 kV. Transmission electron microscopy (TEM) was performed at 200 kV (JEM-2100 Plus, JEOL Ltd, Japan) for further analysis. To determine the average particle size (d) from the SEM images, more than 100 particles were measured (Fig. S1†). The crystal structures of the samples were investigated using X-ray diffraction (XRD; Ultima IV, Rigaku, Japan) with a Cu target (45 kV, 40 mA, λ = 1.54 Å) in the range of 10–60°, with a step size of 0.02° and a scan rate of 2° min^{-1}. The pore volume and surface area were calculated using the Brunauer–Emmett–Teller (BET) method based on the N_2 adsorption–desorption isotherms (77 K, liquid nitrogen temperature) (BELSORP mini-2, MicrotracBEL Corp., Japan). Prior to the measurement, the sample was degassed at 180 °C under vacuum for 3 h. X-ray photoelectron spectroscopy (XPS) was

conducted using a spectrometer (K-alpha, Thermo U. K., USA) equipped with an Al K_α X-ray source. Raman spectra were collected over the range of 1000–2000 cm^{-1} (Labram Aramis, Horiba, Japan). Fourier transform infrared spectroscopy (FT-IR; Cary 630, Agilent, USA) was conducted in transmission mode in the range of 4000–400 cm^{-1} to identify the surface functional groups.

2.5 Electrochemical measurements

Electrochemical measurements were performed using a VSP potentiostat in a three-electrode system. The counter electrode was made of a Pt wire, the reference electrode was Ag/AgCl, and the working electrode was immersed in 1 M H_2SO_4 electrolyte. The working electrode material was prepared by mixing 8 mg of the active materials, 1 mg of PVDF, and 1 mg of carbon black in NMP. The resulting homogeneous slurry was drop-cast onto a 1 cm × 1 cm graphite electrode with a mass loading of 1.0 mg cm^{-2} and dried at 60 °C for 12 h. The electrochemical properties were characterized using cyclic voltammetry (CV), galvanostatic charge–discharge (GCD), and electrochemical impedance spectroscopy (EIS). The EIS tests were performed within the frequency range of 0.01 Hz–100 kHz, applying an amplitude of 10 mV. The cyclability of the electrode was investigated using GCD cycles at 10 A g^{-1}. The specific capacitance was calculated from the CV and GCD curves using the following equations:

$$C_{g,CV} \left(\text{F g}^{-1}\right) = \frac{\int I\text{d}v}{2 \times v \times \Delta V \times m} \tag{1}$$

$$C_{g,GCD} \left(\text{F g}^{-1}\right) = \frac{I \times \Delta t}{\Delta V \times m} \tag{2}$$

where C_g is the specific capacitance (F g^{-1}), $I\text{d}v$ is the integrated area of the CV curve, v is the scan rate (mV s^{-1}), ΔV is the potential window (V), m is the mass of the active material (mg), I is the discharging current (mA), and Δt is the discharge time (s). To investigate the electrochemical properties in greater detail, a flexible solid-state symmetric supercapacitor was assembled using the same mass loading as that employed in the single-electrode configuration. The specific energy (SE; Wh kg^{-1}) and specific power (SP; W kg^{-1}) of the supercapacitors were calculated using the following equations:

$$\text{SE} = \frac{1}{2} C\Delta V^2 \times \frac{1}{3.6} \tag{3}$$

$$\text{SP} = \frac{3600 \times \text{SE}}{t} \tag{4}$$

where C (F g^{-1}) is the specific capacitance of the total symmetrical system, ΔV (V) is the voltage change during the discharge process, and t (s) is the discharge time.

3. Results and discussion

In this study, ZIF-8 nanocrystals were synthesized as an N-doped carbon precursor (Fig. 1). Briefly, nucleation seeds were generated under aqueous solution conditions *via* the coordination between Zn^{2+} and 2-methylimidazole (2-mIm). Thereafter, these nucleation seeds grew into ZIF-8 nanocrystals, forming a $Zn–N_4$ complex through crystal growth. The synthesized ZIF-8 nanocrystals exhibited a very high uniformity (Fig. 2a) and a rhombic dodecahedral shape (Fig. 2b). The nucleation stage occurred within seconds;[32] therefore, to ensure homogeneous seed formation at the beginning of the synthesis, the Zn solution was added to the 2-mIm solution under vigorous stirring. To achieve the formation of ZIF-8 nanocrystals in water, the quantity of 2-mIm should be higher than that of Zn^{2+}. In contrast, adding the 2-mIm solution to Zn solution at a low stirring speed results in inhomogeneous seed formation and irregular crystal growth over time (denoted as ZIF-8-n, Fig. S2†).

To regulate the particle size of the uniform ZIF-8 nanocrystals, the synthesis conditions were adjusted (Table S1†). Achieving smaller particles requires the formation of many nuclei followed by rapid crystal growth;[34] thus, we increased the duration for which the Zn solution was added to the 2-mIm solution. In contrast, increasing the water content in each solution and decreasing the molar ratio between the zinc precursor and 2-mIm to decrease the crystal growth after the formation of a few nuclei led to saturation, resulting in the formation of larger particles.[33,35]

As shown in Fig. S3,† the modification of the synthesis conditions enabled the successful synthesis of ZIF-8 nanocrystals with sizes of 147, 346, 512, 750, and 915 nm (the monodisperse sizes of ZIF-8 are labeled from ZIF-8-m1 to ZIF-8-m5, in the order of the smallest to the largest size). The crystalline structure and chemical functionalities of the synthesized ZIF-8 samples were characterized using X-ray diffraction (XRD) and Fourier transform infrared (FT-IR) analysis (Fig. S4a and S4b†). Peaks corresponding to the (110), (200), (211), (220), (310), and (222) crystal planes are observed at 2θ values of 7.3, 10.4, 12.7, 14.7, 16.4, and 18.0°, respectively (Fig. S4a†). The bending peaks both in-plane and out-of-plane were observed within the ranges of 900–1350 cm^{-1} and below 800 cm^{-1}, respectively (Fig. S4b†). In addition, a distinct peak observed at 417 cm^{-1} was linked to the Zn–N bond, further confirming the formation of the intended framework. Additionally, a complex band was observed between 1350 and 1500 cm^{-1}, which corresponds to the overall ring stretching vibrations, aligning with the structural features of ZIF-8. Peaks associated with the aromatic and aliphatic C–H stretching modes of the imidazole rings, as well as the C=N stretching vibration, were observed at 1580, 3138, and 2929 cm^{-1}, respectively. The XRD peaks and FT-IR peaks of all the samples were nearly identical, confirming that the variations in synthesis conditions exerted no effect on the crystalline structure or surface functionalities, except for changes in the sample size.

The pyrolysis of the ZIF-8 nanocrystals at 900 °C under a nitrogen flow (Fig. 2a and b) transformed the nanocrystals into ZIF-8-C samples. High-magnification transmission electron microscopy (TEM) images revealed that the particles were composed of disordered (amorphous) carbon (Fig. 2c), and the
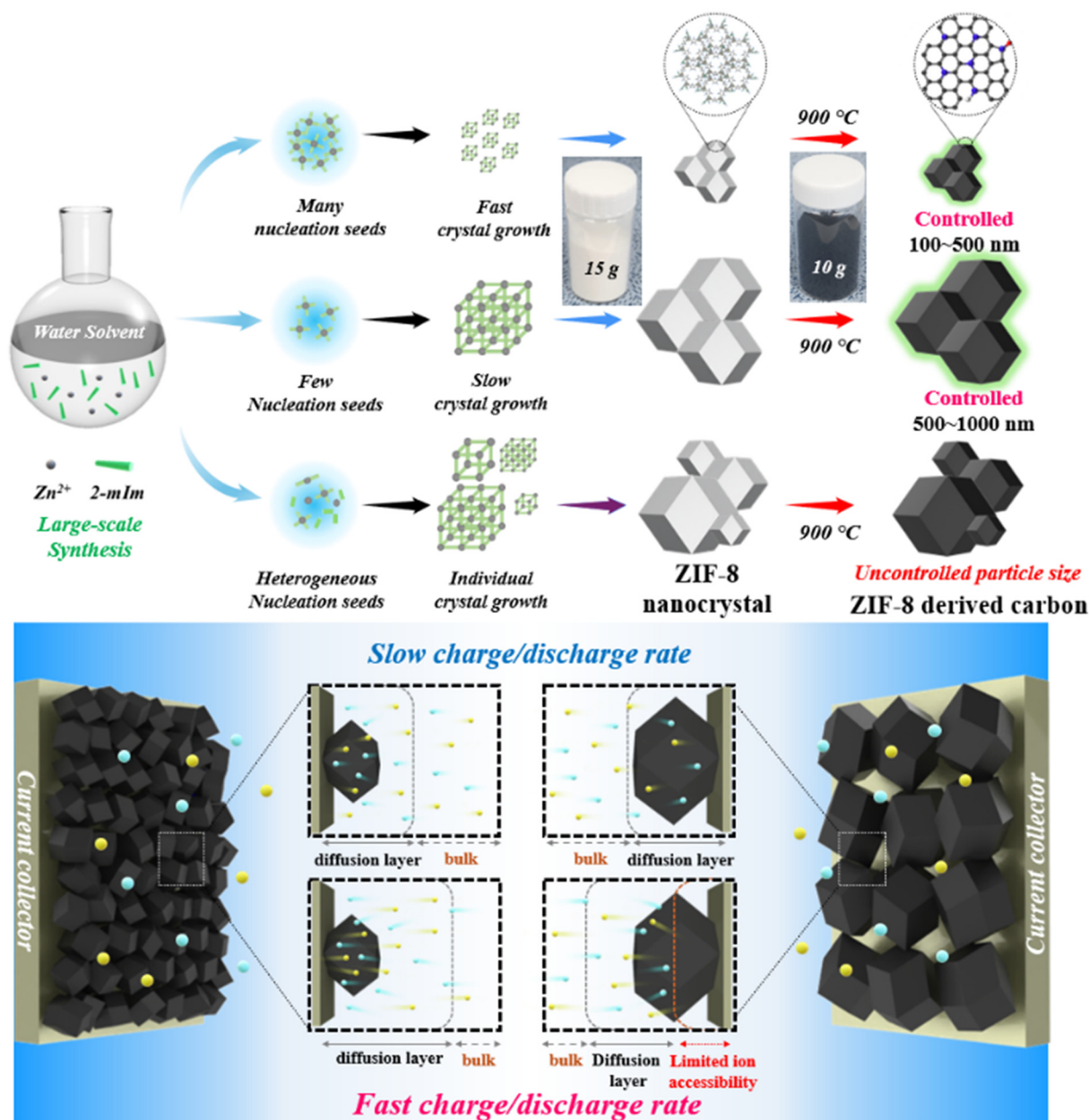
Fig. 1 Schematic of the preparation methods for ZIF-8-C with various particle sizes and size distributions, and the effect of particle size on the supercapacitor performance.

TEM-energy dispersive X-ray spectroscopy (EDS) analysis confirmed the successful nitrogen doping and the removal of residual Zn through HCl washing (Fig. 2d). The scanning electron microscopy (SEM) and TEM images of the ZIF-8-C samples after carbonization revealed that they retained their original rhombic dodecahedron morphology and exhibited the same high uniformity as the parent ZIF-8 (Fig. 2e–n), whereas ZIF-8-C-n exhibited a wider particle size distribution (Fig. 2o and p).

After carbonization, the size of all samples decreased by approximately 20–30%, due to the decomposition of organic ligands and the loss of metal ions (Zn), which resulted in a

reduction in mass and volume. The carbon structure also becomes denser, contributing to the size reduction. In particular, the sizes of ZIF-8-C-m1, ZIF-8-C-m2, ZIF-8-C-m3, ZIF-8-C-m4, and ZIF-8-C-m5 reduced from 147, 346, 512, 750, and 915 nm to 113, 270, 384, 562, and 732 nm, respectively (Fig. 3a). The degrees of crystallinity and graphitization of the carbon samples were evaluated using XRD and Raman spectroscopy (Fig. 3b and c). Two broad diffraction peaks were observed in the XRD patterns at 25 and 44°, which correspond to the (002) and (101) planes of graphite, respectively, and the characteristic peaks of ZIF-8 were notably absent. These observations indicate the thermal transformation of ZIF-8 nanocrys-
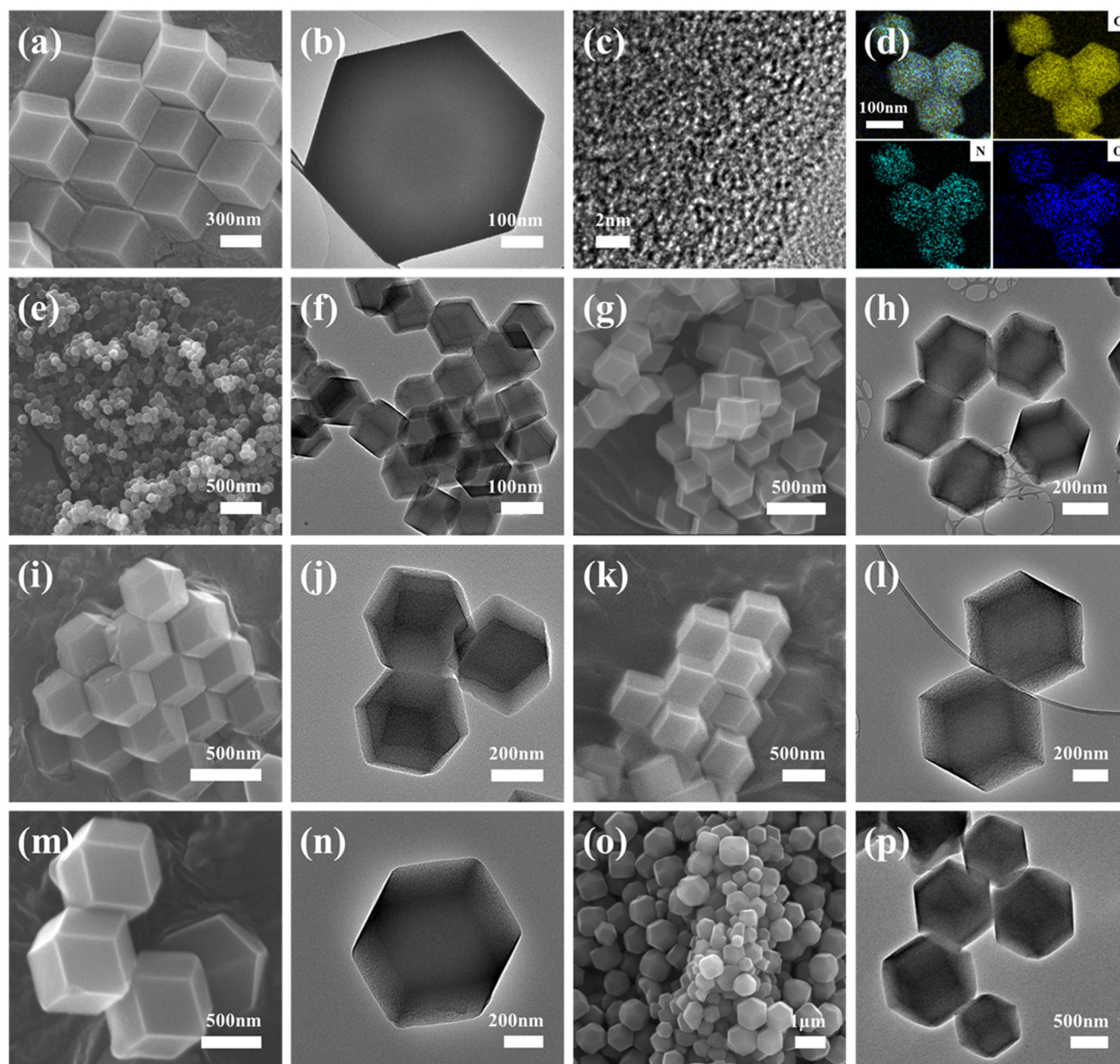
Fig. 2 (a) Scanning electron microscopy (SEM) and (b) transmission electron microscopy (TEM) images of ZIF-8 nanocrystals. (c) High-magnification TEM image and (d) TEM-energy dispersive X-ray spectroscopy (EDS) mapping of ZIF-8-C-m1. SEM and TEM images of (e and f) ZIF-8-C-m1, (g and h) ZIF-8-C-m2, (i and j) ZIF-8-C-m3, (k and l) ZIF-8-C-m4, (m and n) ZIF-8-C-m5, and (o and p) ZIF-8-C-n.

tals into porous carbon materials. In the Raman spectra of all carbon samples, distinctive D- and G-bands were observed at 1350 and 1580 cm^{-1}, corresponding to the vibrations of sp^3-bonded carbon atoms or defects, and sp^2-bonded carbon atoms in ordered graphitic structures, respectively.[36]

The graphitization degree can be assessed using the intensity ratio of the D-band to the G-band (I_D/I_G ratio). All samples exhibited similar I_D/I_G ratios ranging between 0.95 and 1.14. The uniform ZIF-8-C-m samples exhibited higher levels of crystallinity and graphitization compared to ZIF-8-C-n (Fig. 3d), indicating their enhanced electrical conductivity and improved

ion diffusion, which contribute to their superior electrochemical performance.[37] The Brunauer–Emmett–Teller (BET) surface area and porosity were analyzed using N$_2$ adsorption–desorption isotherms to determine key characteristics of the samples. The ZIF-8 nanocrystals exhibited a type-I adsorption isotherm, indicating a dominant micropore structure, which was further confirmed by its pore size distribution. As shown in Fig. S5 and Table S2,† the surface area increases as the particle size decreases. The ZIF-8-n sample exhibited a larger surface area than ZIF-8-m5, which was attributed to the presence of mixed small particles.
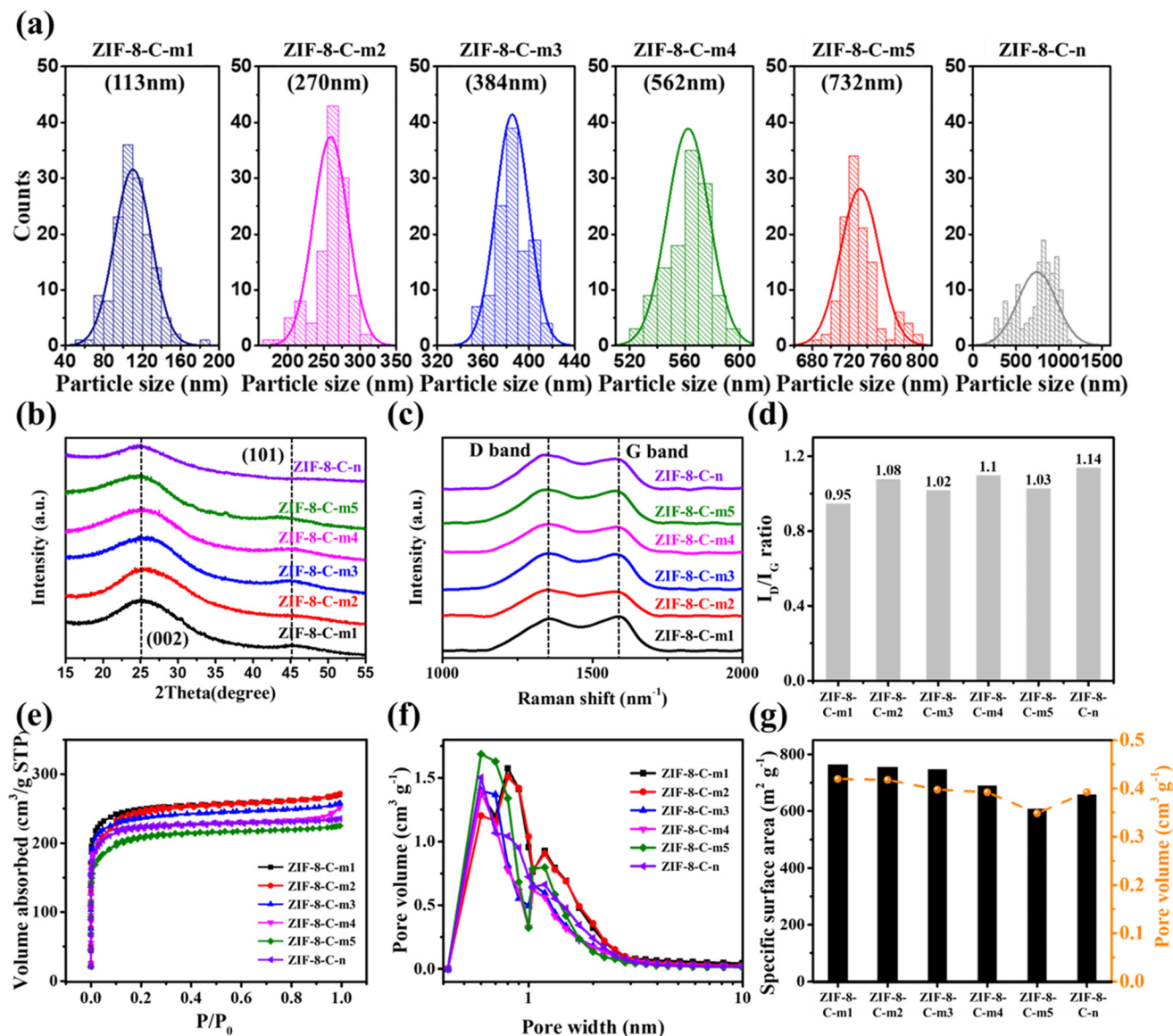
Fig. 3 (a) Particle size distribution, (b) XRD patterns, (c) Raman spectra, (d) intensity ratio of the D-band to the G-band (I_D/I_G ratio), (e) N_2 adsorption–desorption isotherms, (f) pore size distribution, and (g) Brunauer–Emmett–Teller (BET) surface area and pore volume of ZIF-8-C samples.

After carbonization, the carbon samples maintained a type-I adsorption isotherm, but the high carbonization temperature slightly reduced the surface area owing to the initial pore collapse (Fig. 3e). The pore size distribution indicates that the ZIF-8-C samples are predominantly composed of micropores, with only a very small amount of mesopores present (Fig. 3f). Among the carbon samples, ZIF-8-C-m1 exhibited the highest specific surface area (763 m² g⁻¹), which can be attributed to the increase in the surface area of the material consisting of smaller particles. The BET specific surface area (S_{bet}), total pore volume (V_{total}), and average pore diameter (D_{avg}) of the samples are summarized in Table 1 and Fig. 3g.

Surface elemental mapping analysis of the samples was conducted using X-ray photoelectron spectroscopy (XPS) analysis (Fig. 4). The XPS survey spectra and atomic contents of

Table 1 BET analysis results of the ZIF-8-derived carbon samples with different particle sizes

Sample	S_{bet} (m² g⁻¹)	V_{total} (cm³ g⁻¹)	V_{micro} (cm³ g⁻¹)	D_{avg} (nm)
ZIF-8-C-m1	763	0.42	0.38	2.14
ZIF-8-C-m2	755	0.42	0.38	2.21
ZIF-8-C-m3	748	0.40	0.37	2.10
ZIF-8-C-m4	691	0.39	0.36	2.12
ZIF-8-C-m5	608	0.35	0.32	2.11
ZIF-8-C-n	659	0.39	0.36	2.28

the ZIF-8-C samples revealed the disappearance of the Zn peak and content, observed at 1021.6 eV (Fig. 4a and Table S3†), indicating the successful removal of residual Zn through HCl
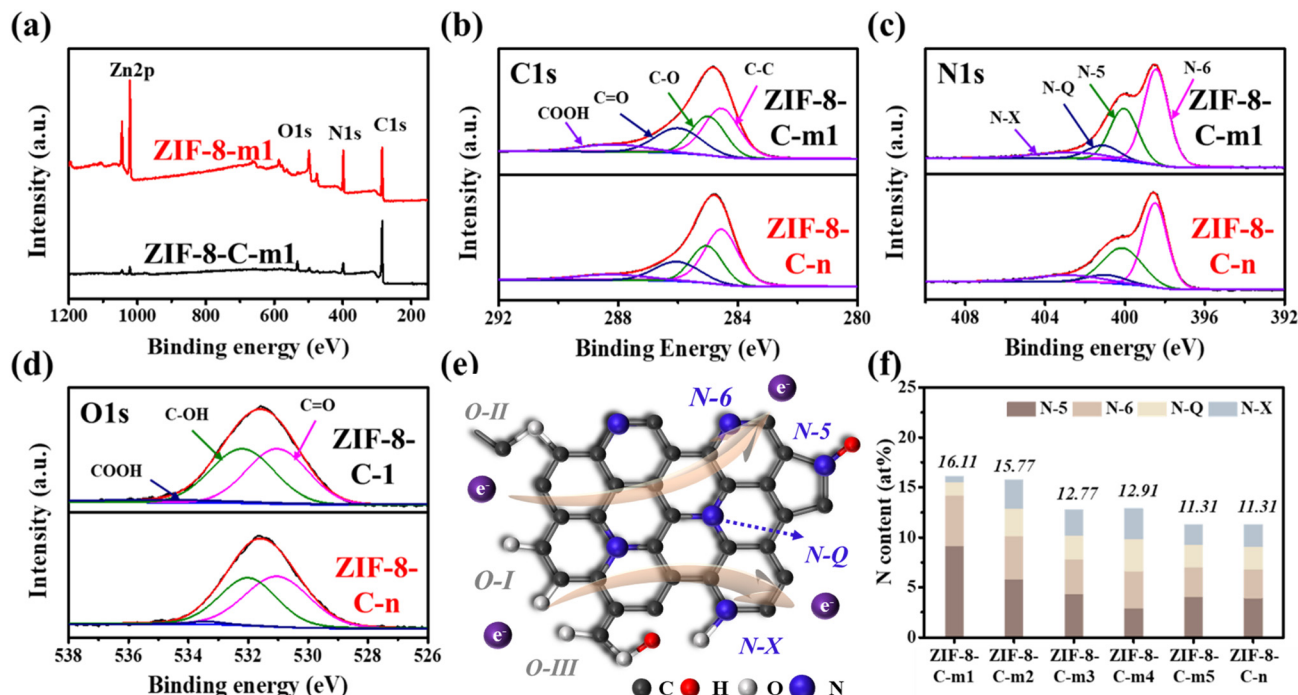
Fig. 4 (a) XPS profiles of ZIF-8-m1 and ZIF-8-C-m1; (b) C 1s, (c) N 1s, and (d) O 1s XPS profiles of ZIF-8-C-m1 and ZIF-8-C-n; (e) schematic model of the oxygen and nitrogen groups on the carbon samples; and (f) nitrogen atom content in all carbon samples.

washing after carbonization. This confirmed that the ZIF-8-derived carbon was successfully obtained. Additionally, the presence of carbon (284.8 eV), nitrogen (398.6 eV), and oxygen (531.6 eV) atoms was confirmed in all the ZIF-8-C samples (Fig. S6–8†), and the specific contents for each sample are summarized in Table S3.† The C 1s spectra could be deconvoluted into four different peaks: C–C (284.5 eV), C–O (285.2 eV), C=O (286.2 eV), and COOH (288.5 eV) (Fig. 4b).[38] For nitrogen, four types of peaks were observed in the N 1s spectra at 398.5, 400, 401.5, and 403 eV, corresponding to pyridinic N (N-6), pyrrolic N (N-5), graphitic (quaternary) N (N-Q), and oxidized N (N-X), respectively (Fig. 4c).[39] The O 1s spectra were fitted with three component peaks, corresponding to O-I (–C=O, 531 eV), O-II (–C–OH, 532 eV), and O-III (–COOH, 533.5 eV) (Fig. 4d).[40] The O-I groups can provide pseudocapacitive sites in acid electrolytes, while O-II and O-III can improve the wettability of carbon materials.[41] Nitrogen and oxygen-containing functional groups, which contribute to the improvement of electrochemical performance, are depicted in Fig. 4e.[42] In the samples, the N-6 atoms were bonded with two carbon atoms with sp^2 hybridization and the N-5 atoms were integrated into a five-membered ring of carbon atoms, with the edge N (N-5 and N-6) contributing to pseudocapacitive sites for energy storage.[43–45] Additionally, the N-Q atoms were bonded to three carbon atoms with sp^3 hybridization and N-X represented an oxidized pyridinic nitrogen atom.[46] It is known that N-Q and N-X can improve the conductivity of the electrode material and electron transportation.[47] The carbon samples exhibited nitrogen contents exceeding 10% of the total elements (Fig. 4f),

and this high nitrogen content enhanced the electron transport efficiency, resulting in high-performance supercapacitors.

To explore the effects of particle size on the electrochemical properties, cyclic voltammetry (CV) and galvanostatic charge–discharge (GCD) tests were conducted in a three-electrode system containing 1 M H_2SO_4 solution. All samples exhibited quasi-rectangular CV curves without redox peaks, representing the typical electrical double-layer behavior of the electrodes (Fig. 5a and S9†).[48] Additionally, no IR drop was observed in the GCD curve, indicating low internal resistance (Fig. 5b and S10†). The CV and GCD curves revealed that among the samples, ZIF-8-C-m1 exhibited the highest specific capacitance, which decreased with increasing particle size (Tables S4 and S5†). In electrochemical double-layer capacitors (EDLCs), energy storage primarily involves ion accumulation at the electrode and is significantly affected by the surface area of the electrode material. A higher surface area enables the storage of a greater number of ions during charging and discharging, resulting in improved supercapacitor performance. In particular, the GCD curves at 1 A g^{-1} revealed that the specific capacitance increased in the following order: ZIF-8-C-m5 (170.47 F g^{-1}) < ZIF-8-C-m4 (183.27 F g^{-1}) < ZIF-8-C-m3 (196.54 F g^{-1}) < ZIF-8-C-m2 (201.54 F g^{-1}) < ZIF-8-C-m1 (206.4 F g^{-1}) with respect to the S_{bet} of the particles (Fig. 5c). The charge–discharge capability was determined not only by the particle surface area but also by the accessibility of ions to pore channels. At low scan rates or current densities, electrolyte ions are provided with sufficient time to effectively diffuse into the active material. In contrast, at high current densities, the time
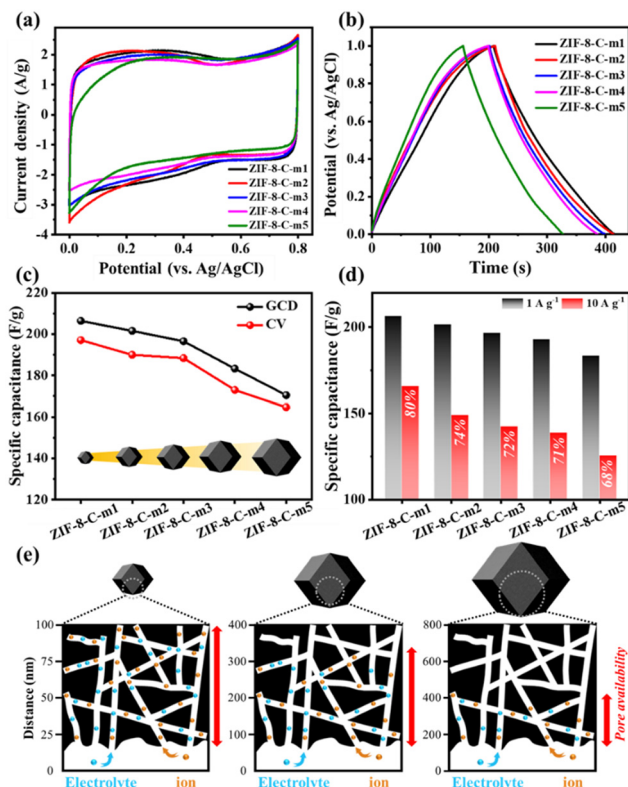
Fig. 5 (a) CV curves (10 mV s^{-1}) and (b) GCD curves (1 A g^{-1}) of the uniform ZIF-8-C samples with different particle sizes. (c) Relative specific capacitance of the uniform ZIF-8-C samples with different particle sizes and (d) at different current densities. (e) Schematic representation of electrolyte ion accessibility differences according to particle size.

for electrolyte ion diffusion was insufficient, leading to a sharp decrease in capacitance. Accordingly, ZIF-8-C-m1 exhibited a capacitance of 206.4 F g^{-1} at 1 A g^{-1}, which decreased by 20% to 165.6 F g^{-1} at 10 A g^{-1} (Fig. 5d). In contrast, despite the similar specific surface area of ZIF-8-C-m2 and ZIF-8-C-m1, the capacitance of ZIF-8-C-m2 was significantly lower (201.54 and 149.1 F g^{-1} at 1 and 10 A g^{-1}, respectively, representing a 26% decrease). This decreasing trend increased with increasing particle size. This indicates that larger particles may not fully utilize deep pores at high scan rates or current densities, thereby limiting the accessibility of electrolyte ions. In contrast, sufficiently small particles can maximize energy storage in EDLCs even at high scan rates or current densities owing to efficient electrolyte ion diffusion and pore accessibility (Fig. 5e).

A comprehensive comparison of the electrochemical performance of samples with uniform and non-uniform carbon particle sizes was conducted. The area under the CV curves and the discharge time estimated from the GCD curves of ZIF-8-C-m1 (206.4 F g^{-1} at 1 A g^{-1}) are larger than those of ZIF-8-C-n (155.34 F g^{-1} at 1 A g^{-1}), implying the higher capacitance of ZIF-8-C-m1 (Fig. 6a and b). Moreover, ZIF-8-C-m5, which exhibited the smallest capacitance among the uniform samples, maintained a high charge storage capacity compared to ZIF-8-C-n across a range of current densities from 1 to 10 A

g^{-1} (Fig. 6c). Nyquist plots of ZIF-8-C samples were obtained using EIS in the frequency range of 0.01 Hz–100 kHz (Fig. 6d and S11†). The equivalent series resistance (R_s), encompassing the resistances of the current collector, electrode, electrolyte, intrinsic resistance, and solution resistance, is inferred by the intercept of the semicircle on the real axis. The charge transfer resistance (R_{ct}), which signifies the charge transfer at the electrode–electrolyte interface, is represented by the diameter of the semicircle. Additionally, the Warburg region, situated between the semicircle and the long tail, highlights the diffusion barrier of the electrolyte ions.[49,50] The R_s value of each sample was approximately 1.0 Ω; however, the R_{ct} values of the samples varied significantly (Table S6†). Samples characterized by a uniform particle distribution exhibited lower R_s and R_{ct} values compared to those with ZIF-8-C-n, indicating enhanced kinetic performance and ion diffusion. The R_{ct} values of ZIF-8-C-m1 and ZIF-8-C-n were 0.2124 and 0.5718 Ω, respectively, representing an approximately three-fold difference. This variation highlights the effectiveness of small, evenly distributed particles in improving the electrode structure, thus significantly reducing the resistance at the electrode–electrolyte interface.[51] After 10 000 cycles at 10 A g^{-1}, ZIF-8-C-m1 retained 99.65% of its initial specific capacitance, and the first and last five GCD curves were almost identical, demonstrating high cycling stability (Fig. 6e and Table S7†). As observed in Fig. 6f, the uniform ZIF-8-C samples exhibited superior electrochemical performance compared to other references using ZIF-8-derived carbons of varying sizes, owing to their packing structure resulting from high uniformity. To understand the arrangement of electrode materials on the current collector, we analyzed the SEM images of the cross-sections of the electrode (Fig. 6g–l). For the ZIF-8-C-m1 and ZIF-8-C-m5 electrodes, the stacking structure exhibited high uniformity with carbon black and PVDF being evenly distributed. In contrast, in the case of ZIF-8-C-n, where small and large carbon particles are randomly mixed, the aggregation of PVDF with carbon black makes achieving an ordered packing structure inherently challenging. This is because the random size of the carbon particles hinders the systematic arrangement of the particles, which is necessary for the optimized packing structure of the electrode. These variations in the electrode packing structure significantly impacted electron transport and ion diffusion, thereby influencing the overall performance of the supercapacitor. Accordingly, despite its higher specific surface area, ZIF-8-C-n exhibits lower supercapacitor performance relative to ZIF-8-C-m5, which may be attributed to the differences in the closely well-packed structure of the electrode material (Fig. S12†).

To further evaluate the electrochemical performance, a flexible solid-state symmetric supercapacitor was assembled with two identical electrode materials and PVA/H$_3$PO$_4$ gel electrolytes (Fig. 7a). The exploration of the operating voltage window, as illustrated in Fig. 7b and Fig. S13,† revealed that polarization reactions occurred when the device's voltage window exceeded 1.6 V. To prevent electrolyte decomposition and ensure stability, the operating potential was set at 0.0–1.4
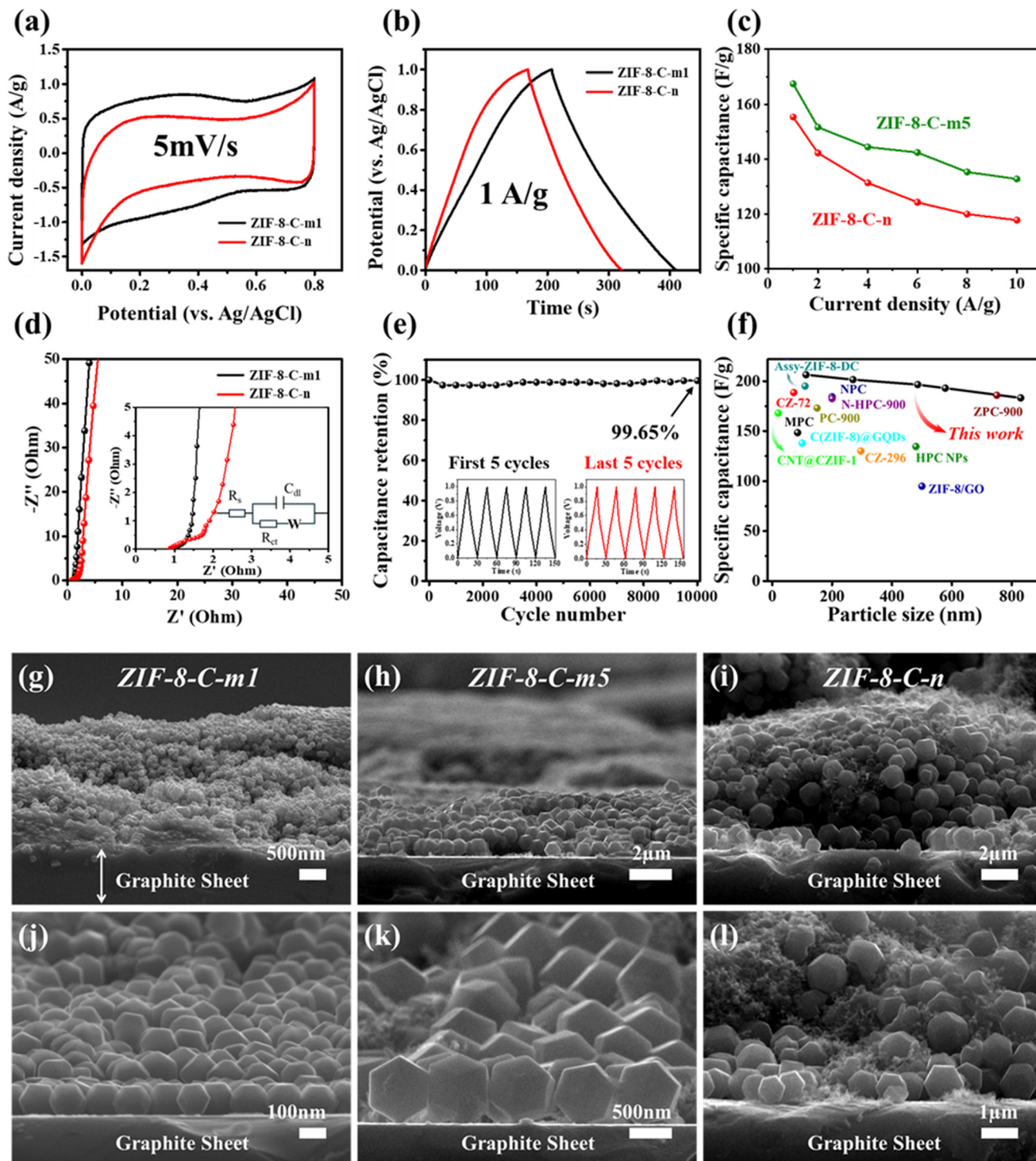
Fig. 6 (a) CV curves, (b) GCD curves, (c) capacitance retention at different current densities, and (d) Nyquist plots of ZIF-8-C-m1, ZIF-8-C-m5, and ZIF-8-C-n (inset: Randles equivalent circuit); (e) cycling stability of ZIF-8-C-m1 at 10 A g^{-1} across 10 000 cycles; and (f) relative capacitance of ZIF-8-derived carbon samples of varying sizes. Low- and high-magnification SEM cross-sectional images of (g and j) ZIF-8-C-m1, (h and k) ZIF-8-C-m5, and (i and l) ZIF-8-C-n.

V. Fig. 7c and Fig. S14† show that despite the scan rates increasing to 10, 20, 50, 100, and 200 mV s^{-1}, the CV curves maintained a quasi-rectangular shape, indicating stable EDLC characteristics. The GCD curves retained an isosceles triangu-

lar shape at various current densities, further confirming ideal EDLC behavior (Fig. 7d and Fig. S15†). The specific capacitance of the symmetric device was determined from the discharge curves, taking into account the total mass of active
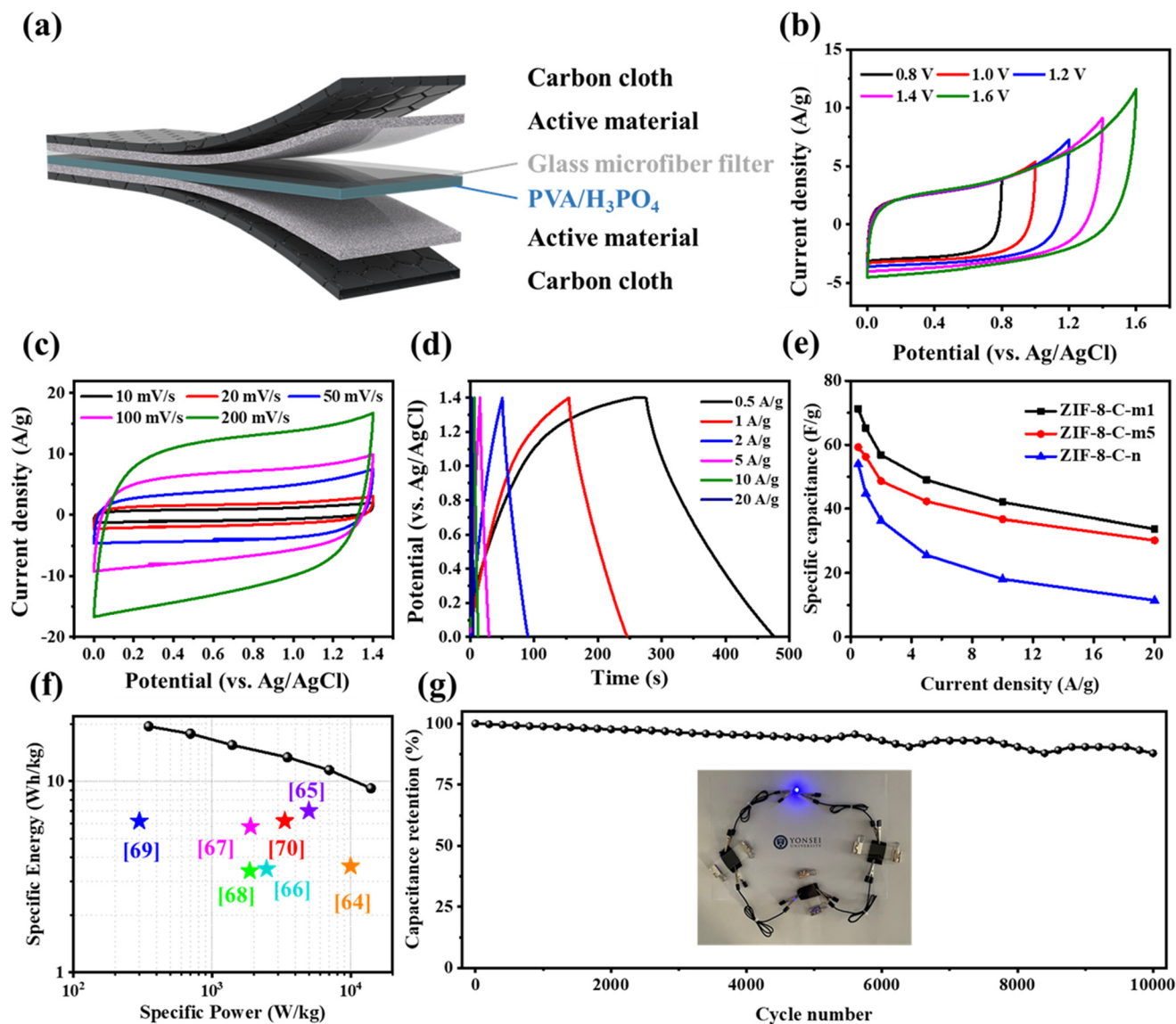
Fig. 7 (a) Schematic illustration of the flexible solid-state supercapacitor device. (b) CV curves at 50 mV s^{-1} in different voltage windows, (c) CV curves at various scan rates (10–200 mV s^{-1}), and (d) GCD curves at various current densities (0.5–20 A g^{-1}) for ZIF-8-c-m1. (e) Capacitance retention at various current densities and (f) Ragone plot of ZIF-8-c-m1 and other representative porous carbon electrodes. (g) Cycling stability of ZIF-8-C-m1 at 10 A g^{-1} over 10 000 cycles. Inset: three series-connected devices lighting an LED indicator.

materials present on both electrodes (Fig. 7e). Consistent with the results obtained in the three-electrode configuration, the uniform particle samples showed higher capacitance with decreasing particle size (ZIF-8-C-m1: 71.3 F g^{-1} and ZIF-8-C-m5: 59.3 F g^{-1} at 0.5 A g^{-1}), whereas the non-uniform particle sample (ZIF-8-C-n) exhibited the lowest capacitance (54.0 F g^{-1} at 0.5 A g^{-1}) across all current densities. The Ragone plot was used to assess specific power and energy density, showing that ZIF-8-C-m1 achieved an energy density of 19.4 W h kg^{-1} and a specific power of 350 W kg^{-1} at 0.5 A g^{-1}, comparable to those of previously reported nanoporous carbons for symmetric supercapacitors (Fig. 7f).[52–58] Additionally, a capacity retention of 87.9% after 10 000 cycles demonstrates the high stability and exceptional electrochemical performance of the symmetric

supercapacitor. *Ex situ* XRD analysis performed on the electrodes post-cycling confirmed that the characteristic diffraction peaks of the pristine material were retained, indicating the preservation of the structural integrity of the electrodes throughout the long-term cycling process (Fig. S16†). In practice, three supercapacitor devices were connected in series to successfully power a green LED light, as shown in the inset of Fig. 7g.

4.   Conclusions

This study aims to assess the effects of the particle size and uniformity of a ZIF-8-C nanostructure on its electrochemical

properties. To achieve this, we synthesize monodisperse ZIF-8 nanocrystals of varying sizes and with non-uniform particle distributions. After the carbonization of the ZIF-8 nanocrystals, the ZIF-8-C samples maintain their initial size distributions, while also exhibiting similar specific surface areas, nitrogen content, and degrees of graphitization. Our findings reveal that the charge storage capacity increases as the particle size decreases. Additionally, compared to samples with smaller particles, samples with larger particles exhibit a greater reduction in capacitance compared to their initial values at high scan rates or current densities. This observation is attributed to the diminished availability of internal pores in samples with larger particles at fast charge/discharge rates, potentially impeding ion diffusion. Additionally, we examine the electrochemical performance of samples with non-uniform particle sizes in comparison to monodisperse ZIF-8-C. Uniform particle sizes correspond to lower resistance values in the EIS analysis results. This outcome can be attributed to the ordered packing structure owing to the uniform particle sizes, which facilitates effective electron pathways. Overall, our study offers valuable insights into the impact of the nanostructure and particle size on energy storage using nanomaterial-based carbon. Importantly, these findings can serve as a foundational reference for future research on electrochemical applications using nanoporous carbons.

Author contributions

Donggyun Kim: writing – original draft, investigation, data curation, and conceptualization. Jinhyeon Park: investigation and data curation. Seonghyeon Jung: investigation and data curation. Jieun Jang: investigation and data curation. Minsu Han: investigation and data curation. Minjun Kim: investigation and data curation. Wenkai Zhu: data curation and investigation. Woo-Jin Song: investigation and data curation. Yusuke Yamauchi: data curation and investigation. Jeonghun Kim: writing – review & editing, supervision, investigation, funding acquisition, and conceptualization.

Data availability

The data that support the findings of this study are available from the corresponding author upon reasonable request.

Conflicts of interest

There are no conflicts to declare.

Acknowledgements

References

1 J. Liu, J. Wang, C. Xu, H. Jiang, C. Li, L. Zhang, J. Lin and Z. X. Shen, *Adv. Sci.*, 2018, **5**, 1700322.

2 Z. Yang, J. Zhang, M. C. W. Kintner-Meyer, X. Lu, D. Choi, J. P. Lemmon and J. Liu, *Chem. Rev.*, 2011, **111**, 3577–3613.

3 G. L. Soloveichik, *Annu. Rev. Chem. Biomol. Eng.*, 2011, **2**, 503–527.

4 B. Dunn, H. Kamath and J.-M. Tarascon, *Science*, 2011, **334**, 928–935.

5 L. Zhang, X. Hu, Z. Wang, F. Sun and D. G. Dorrell, *Renewable Sustainable Energy Rev.*, 2018, **81**, 1868–1878.

6 C. Liu, Z. Yu, D. Neff, A. Zhamu and B. Z. Jang, *Nano Lett.*, 2010, **10**, 4863–4868.

7 C. Choi, H. J. Sim, G. M. Spinks, X. Lepró, R. H. Baughman and S. J. Kim, *Adv. Energy Mater.*, 2016, **6**, 1502119.

8 J. Pokharel, A. Gurung, A. Baniya, W. He, K. Chen, R. Pathak, B. S. Lamsal, N. Ghimire and Y. Zhou, *Electrochim. Acta*, 2021, **394**, 139058.

9 Z. Li, K. Xu and Y. Pan, *Nanotechnol. Rev.*, 2019, **8**, 35–49.

10 P. Z. Moghadam, A. Li, S. B. Wiggin, A. Tao, A. G. P. Maloney, P. A. Wood, S. C. Ward and D. Fairen-Jimenez, *Chem. Mater.*, 2017, **29**, 2618–2625.

11 W. Zhu, M. Han, D. Kim, J. Park, H. Choi, G. Kwon, J. You, S. Li, T. Park and J. Kim, *J. Water Process Eng.*, 2023, **53**, 103620.

12 C. Wang, J. Kim, J. Tang, M. Kim, H. Lim, V. Malgras, J. You, Q. Xu, J. Li and Y. Yamauchi, *Chem*, 2020, **6**, 19–40.

13 Y. Pan, Y. Liu, G. Zeng, L. Zhao and Z. Lai, *Chem. Commun.*, 2011, **47**, 2071.

14 B. Chen, Z. Yang, Y. Zhu and Y. Xia, *J. Mater. Chem. A*, 2014, **2**, 16811–16831.

15 D. Kim, J. Park, J. Park, J. Jang, M. Han, S. H. Lim, D. Y. Ryu, J. You, W. Zhu and Y. Yamauchi, *Small Methods*, 2024, 2400236.

16 W. Zhu, M. Han, D. Kim, Y. Zhang, G. Kwon, J. You, C. Jia and J. Kim, *Environ. Res.*, 2022, **205**, 112417.

17 C. Wang, J. Kim, J. Tang, J. Na, Y. M. Kang, M. Kim, H. Lim, Y. Bando, J. Li and Y. Yamauchi, *Angew. Chem.*, 2020, **132**, 2082–2086.

18 R. Ahmad, U. A. Khan, N. Iqbal and T. Noor, *RSC Adv.*, 2020, **10**, 43733–43750.

19 W. Zhu, D. Kim, M. Han, J. Jang, H. Choi, G. Kwon, Y. Jeon, D. Y. Ryu, S.-H. Lim and J. You, *Chem. Eng. J.*, 2023, **460**, 141593.

20 Y. Zhao, H. Nara, D. Jiang, T. Asahi, S. M. Osman, J. Kim, J. Tang and Y. Yamauchi, *Small*, 2023, **19**, 2304450.

21 B. Ding, Z. Fan, Q. Lin, J. Wang, Z. Chang, T. Li, J. Henzie, J. Kim, H. Dou and X. Zhang, *Small Methods*, 2019, **3**, 1900277.

22 Z. X. Cai, Z. L. Wang, J. Kim and Y. Yamauchi, *Adv. Mater.*, 2019, **31**, 1804903.

23 M. Kim, R. Xin, J. Earnshaw, J. Tang, J. P. Hill, A. Ashok, A. K. Nanjundan, J. Kim, C. Young and Y. Sugahara, *Nat. Protoc.*, 2022, **17**, 2990–3027.

24 M. Rana, J. Kim, L. Peng, H. Qiu, R. Kaiser, L. Ran, M. S. A. Hossain, B. Luo, I. Gentle and L. Wang, *Nanoscale*, 2021, **13**, 11086–11092.

25 J. Kim, J. Kim, J. H. Kim and H. S. Park, *Chem. Eng. J.*, 2020, **382**, 122996.

26 S. Chabi, C. Peng, D. Hu and Y. Zhu, *Adv. Mater.*, 2014, **26**, 2440–2445.

27 S. Zheng, Z. Li, Z.-S. Wu, Y. Dong, F. Zhou, S. Wang, Q. Fu, C. Sun, L. Guo and X. Bao, *ACS Nano*, 2017, **11**, 4009–4016.

28 J. Qian, M. Liu, L. Gan, P. K. Tripathi, D. Zhu, Z. Xu, Z. Hao, L. Chen and D. S. Wright, *Chem. Commun.*, 2013, **49**, 3043.

29 A. Chen, Y. Yu, T. Xing, R. Wang, Y. Zhang and Q. Li, *J. Mater. Sci.*, 2015, **50**, 5578–5582.

30 S. Pilban Jahromi, A. Pandikumar, B. T. Goh, Y. S. Lim, W. J. Basirun, H. N. Lim and N. M. Huang, *RSC Adv.*, 2015, **5**, 14010–14019.

31 Y.-R. Lee, M.-S. Jang, H.-Y. Cho, H.-J. Kwon, S. Kim and W.-S. Ahn, *Chem. Eng. J.*, 2015, **271**, 276–280.

32 M. Jian, B. Liu, R. Liu, J. Qu, H. Wang and X. Zhang, *RSC Adv.*, 2015, **5**, 48433–48441.

33 K. Kida, M. Okita, K. Fujita, S. Tanaka and Y. Miyake, *CrystEngComm*, 2013, **15**, 1794.

34 M. Chang, Y. Wei, D. Liu, J. X. Wang and J. F. Chen, *Angew. Chem., Int. Ed.*, 2021, **60**, 26390–26396.

35 R. Wu, T. Fan, J. Chen and Y. Li, *ACS Sustainable Chem. Eng.*, 2019, **7**, 3632–3646.

36 Y. Dong, S. Zhang, X. Du, S. Hong, S. Zhao, Y. Chen, X. Chen and H. Song, *Adv. Funct. Mater.*, 2019, **29**, 1901127.

37 D. Geng, S. Zhang, Y. Jiang, Z. Jiang, M. Shi, J. Chang, S. Liang, M. Zhang, J. Feng and T. Wei, *J. Mater. Chem. A*, 2022, **10**, 2027–2034.

38 W. Si, J. Zhou, S. Zhang, S. Li, W. Xing and S. Zhuo, *Electrochim. Acta*, 2013, **107**, 397–405.

39 J. Pels, F. Kapteijn, J. Moulijn, Q. Zhu and K. Thomas, *Carbon*, 1995, **33**, 1641–1653.

40 D. Hulicova-Jurcakova, M. Seredych, G. Q. Lu and T. J. Bandosz, *Adv. Funct. Mater.*, 2009, **19**, 438–447.

41 H. Ma, C. Li, M. Zhang, J.-D. Hong and G. Shi, *J. Mater. Chem. A*, 2017, **5**, 17040–17047.

42 B. Xu, D. Zheng, M. Jia, G. Cao and Y. Yang, *Electrochim. Acta*, 2013, **98**, 176–182.

43 R. Liu, L. Pan, J. Jiang, X. Xi, X. Liu and D. Wu, *Sci. Rep.*, 2016, **6**, 21750.

44 X. Yang, D. Wu, X. Chen and R. Fu, *J. Phys. Chem. C*, 2010, **114**, 8581–8586.

45 W.-H. Lee and J. H. Moon, *ACS Appl. Mater. Interfaces*, 2014, **6**, 13968–13976.

46 C. Young, R. R. Salunkhe, J. Tang, C.-C. Hu, M. Shahabuddin, E. Yanmaz, M. S. A. Hossain, J. H. Kim and Y. Yamauchi, *Phys. Chem. Chem. Phys.*, 2016, **18**, 29308–29315.

47 Y. Tan, C. Xu, G. Chen, Z. Liu, M. Ma, Q. Xie, N. Zheng and S. Yao, *ACS Appl. Mater. Interfaces*, 2013, **5**, 2241–2248.

48 W. Li, F. Zhang, Y. Dou, Z. Wu, H. Liu, X. Qian, D. Gu, Y. Xia, B. Tu and D. Zhao, *Adv. Energy Mater.*, 2011, **1**, 382–386.

49 T. Kshetri, D. D. Khumujam, T. I. Singh, Y. S. Lee, N. H. Kim and J. H. Lee, *Chem. Eng. J.*, 2022, **437**, 135338.

50 S. Krishnan, A. K. Gupta, M. K. Singh, N. Guha and D. K. Rai, *Chem. Eng. J.*, 2022, **435**, 135042.

51 M. Kim, X. Xu, R. Xin, J. Earnshaw, A. Ashok, J. Kim, T. Park, A. K. Nanjundan, W. A. El-Said, J. W. Yi, J. Na and Y. Yamauchi, *ACS Appl. Mater. Interfaces*, 2021, **13**, 52034–52043.

52 L. Fang, Y. Xie, Y. Wang, Z. Zhang, P. Liu, N. Cheng, J. Liu, Y. Tu, H. Zhao and J. Zhang, *Appl. Surf. Sci.*, 2019, **464**, 479–487.

53 Z.-S. Wu, W. Ren, D.-W. Wang, F. Li, B. Liu and H.-M. Cheng, *ACS Nano*, 2010, **4**, 5835–5842.

54 M. Usha Rani, K. Nanaji, T. N. Rao and A. S. Deshpande, *J. Power Sources*, 2020, **471**, 228387.

55 B. Duan, X. Gao, X. Yao, Y. Fang, L. Huang, J. Zhou and L. Zhang, *Nano Energy*, 2016, **27**, 482–491.

56 C. Shao, S. Qiu, G. Wu, B. Cui, H. Chu, Y. Zou, C. Xiang, F. Xu and L. Sun, *Carbon Energy*, 2021, **3**, 361–374.

57 C. Shen, R. Li, L. Yan, Y. Shi, H. Guo, J. Zhang, Y. Lin, Z. Zhang, Y. Gong and L. Niu, *Appl. Surf. Sci.*, 2018, **455**, 841–848.

58 J. Yu, N. Fu, J. Zhao, R. Liu, F. Li, Y. Du and Z. Yang, *ACS Omega*, 2019, **4**, 15904–15911.